Reconstruction of Current Flow and Imaging of Current-Limiting Defects in Polycrystalline Superconducting Films

A. E. Pashitski, A. Gurevich, A. A. Polyanskii,*
D. C. Larbalestier, A. Goyal, E. D. Specht, D. M. Kroeger,
J. A. DeLuca, J. E. Tkaczyk

Magneto-optical imaging was used to visualize the inhomogeneous penetration of magnetic flux into polycrystalline $TlBa_2Ca_2Cu_3O_x$ films with high critical current densities, to reconstruct the local two-dimensional supercurrent flow patterns and to correlate inhomogeneities in this flow with the local crystallographic misorientation. The films have almost perfect *c*-axis alignment and considerable local *a*- and *b*-axis texture because the grains tend to form colonies with only slightly misaligned *a* and *b* axes. Current flows freely over these low-angle grain boundaries but is strongly reduced at intermittent colony boundaries of high misorientation. The local (<10-micrometer scale) critical current density J_c varies widely, being up to 10 times as great as the transport J_c (scale of ~1 millimeter), which itself varies by a factor of about 5 in different sections of the film. The combined experiments show that the magnitude of the transport J_c is largely determined by a few high-angle boundaries.

Large-scale applications of high-temperature superconductors (HTSs) require conductors with high critical current densities J_c, which must be polycrystalline by virtue of their long length. Although useful conductor forms of HTSs are all presently made from Bi-Sr-Ca-Cu-O (BSCCO) compounds, there is also a strong interest in thick-film conductors of $YBa_2Cu_3O_x$ and $TlBa_2Ca_2Cu_3O_x$ (Tl-1223) because these materials have lower anisotropy and inherently better flux pinning than BSCCO (*1*). Fabrication in the thick-film form produces a strong *c*-axis texture, which permits high J_c values in polycrystalline films (*2*), particularly when biaxial texturing methods are used (*3*). However, polycrystals have multiple current-limiting mechanisms (*4*), and the macroscopic average $J_c = I_c/A$, derived from the measured critical current I_c and the cross-sectional area A of the superconductor, may contain little useful information about such limits. If defects locally block current flow, then the effective local current-carrying cross section A_e can be significantly less than A, and the macroscopic J_c is then much less than the true local values. Many studies of vortex dynamics and pinning in HTS materials have provided the underlying limit on J_c (*5*). However, when high-angle grain boundaries are present (*6*, *7*), they reduce J_c to a substantially lower level, as do cracks, pores, and other common defects (*8*). The macroscopic value of J_c for conductor forms of BSCCO is determined more by the overall connectivity of the polycrystal than by vortex pinning (*9*); thus, these connectivity-limiting defects must be identified to develop intelligent processing techniques that will minimize or eliminate them.

The experiment described here provides a powerful tool for this task by using magneto-optical (MO) imaging (*10*–*12*) to reveal the current-limiting defects over a large area. We report on the quantitative reconstruction of the local current distribution in polycrystalline HTS films and show that the macroscopic J_c determined on scales of millimeters is mostly determined by highly inhomogeneous current flow $\mathbf{J}(\mathbf{r})$ around defects visible in MO images on scales of 5 to 10 μm. This procedure enabled us to extract the local critical current density distribution $J_c(\mathbf{r})$ and to directly correlate it with the microstructure.

We studied high-J_c Tl-1223 thick films made on polycrystalline yttria-stabilized zirconia (YSZ) substrates (*13*), which can exhibit significant variability in the local value of J_c, even within one batch. Two such 3-μm-thick Tl-1223 films (samples S1 and S2) were made on 1-cm-wide YSZ substrates. Patterned bridges ~160 μm wide dividing the films into four 1-mm-long sections permitted a first test of the J_c variation. The macroscopic transport J_c in S1 measured at 0 T, 77 K, and 1 μV/cm was 86, 88, 19, and 44 kA/cm^2 in sequential sections from voltage taps V0-V1 to V3-V4 (Fig. 1). The maximum value observed was 336 kA/cm^2 for one section of S2 (*2*). We first imaged the two samples in qualitative mode so as to understand whether the variations in J_c had local or global causes and found that the current-carrying capacity of the films was determined by intermittent current-limiting defects.

The MO images were taken at 9 to 77 K in fields of 0 to 120 mT in both field-cooled and zero-field–cooled regimes. A 2-μm-thick, Bi-doped, Y-garnet MO indicator film with in-plane magnetization was placed directly on the Tl-1223 film (*7*). Both samples showed highly nonuniform flux penetration. Sample S1 displayed more defects than did S2, which is consistent with its smaller transport J_c; moreover, the defect density correlated qualitatively with the variation of J_c measured for each individual bridge section.

The MO (Fig. 1A) and microstructural images (Fig. 1B) are shown for a region spanning almost three voltage taps in S1, where the transport J_c at 77 K and 0 T

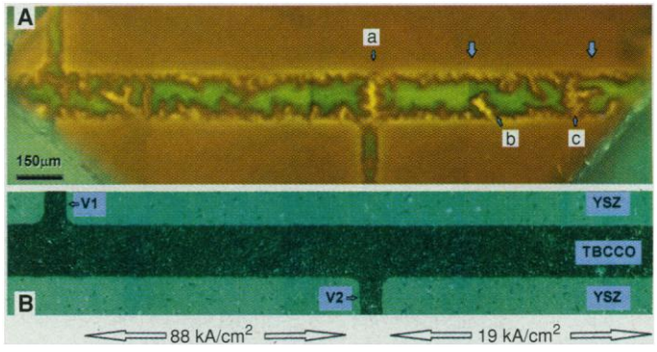

Fig. 1. (**A**) MO image of the bridge after cooling it to 9 K in a perpendicular field of 40 mT and then switching the field off. Green areas show trapped magnetic flux. The large vertical arrows show the region chosen for the current reconstruction of Fig. 3, and a, b, and c indicate characteristic current-limiting defects. The diagonal lines near the image corners are edges of the indicator film. (**B**) Polarized light image of the patterned surface (dark) of the $TlBa_2Ca_2Cu_3O_x$ film S1 on the YSZ substrate. Two voltage taps, V1 and V2, are visible, and V3 is just to the right of the picture. Defects a, b, and c were not visible by either light or scanning electron microscopy.

A. E. Pashitski, A. Gurevich, A. A. Polyanskii, D. C. Larbalestier, Applied Superconductivity Center, University of Wisconsin, Madison, WI 53706, USA.
A. Goyal, E. D. Specht, D. M. Kroeger, Oak Ridge National Laboratory, Oak Ridge, TN 37831, USA.
J. A. DeLuca and J. E. Tkaczyk, General Electric, Schenectady, NY 12301, USA.

*Also at the Institute of Solid State Physics, Russian Academy of Sciences, Chernogolovka, Moscow District, 142432 Russia.

equals 88 kA/cm^2 between taps V1 and V2 and 19 kA/cm^2 between V2 and V3. The MO image was taken at 9 K in zero applied field after the sample was cooled in a perpendicular field of 40 mT. Here the polarizers were set such that the green regions correspond to trapped magnetic flux, and the brighter yellow areas indicate channels of expelled flux along defects. The ragged image indicates some edge-induced defects, but the principal current-limiting defects are clearly those that occur intermittently, as at a, b, and c. However, no contrast was visible at a, b, or c either by polarized light microscopy (Fig. 1B) or higher magnification scanning electron microscopy (*14*).

The local crystallographic orientation was studied by synchrotron x-ray diffraction with a 100-μm-diameter beam (*14*). The film contained colonies as long as 1 to 2 mm, within which individual grains, some 5 to 30 μm in diameter, were only slightly misaligned (Fig. 2). Intermittent high-angle misorientations of 33° and 22° represent boundaries between colonies of these slightly misoriented grains, and they coincide with defects a and c, respectively. The x-ray orientation map suggests that there are two parallel colonies in the vicinity of defect c. Thus, there is a direct correlation between the MO image, the measured transport superconducting properties, and the local grain-to-grain misorientation. The MO image shows that most of the sample has good superconducting properties and strongly suggests that J_c could be significantly increased if the intermittent high-angle colony boundaries could be suppressed.

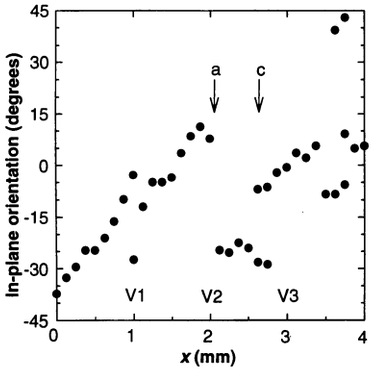

Fig. 2. Variation of the in-plane (*a* and *b*) grain orientation along the bridge measured with a 100-μm diameter synchrotron x-ray diffraction beam. The film is almost perfectly aligned with respect to the *c* axis, and only in-plane misorientations are seen. The majority of the grains are misaligned by only 1° to 5°, but intermittent high-angle boundaries separate these colonies of aligned grains. Two such colony boundaries misoriented by 33° and 22° are shown at a and c. The transport J_c values for different sections at 77 K are 86 kA/cm^2 (V0-V1), 88 kA/cm^2 (V1-V2), 19 kA/cm^2 (V2-V3), and 44 kA/cm^2 (V3-V4).

Because the spatial resolution of the x-ray diffractometry (100 μm) was significantly coarser than that of the MO image (a few micrometers), we reconstructed quantitatively the current flow in the vicinity of the defects. In general, measurement of only one field component, as occurs in an MO experiment, is not enough to reconstruct a three-dimensional (3D) current flow, and additional simplifications are required for quantitative interpretation of MO images on bulk samples (*11*). The situation simplifies for thin films, which have a 2D current density distribution $\mathbf{J}(\mathbf{r})$, thus permitting an inversion of the Biot-Savart law (*15–17*). To reconstruct the inhomogeneous current flow, we developed an inversion procedure, using a fast and stable algorithm that integrates $H_z(x, y)$ over a domain that includes the sample and outer regions. This procedure removes the common restriction to an ideal strip geometry and permits the use of our method for strips with edge irregularities, microbridges of variable width, and other more general cases (*18*).

For detailed reconstruction of the distribution of magnetization sheet currents $\mathbf{J}(\mathbf{r})$, we selected the central segment V2-V3 between the two vertical arrows in Fig. 1A, for which J_c = 19 kA/cm^2. This choice eliminated any significant influence of the magnetization currents circulating in the voltage taps and permitted study near the characteristic defects b and c. The MO image of the chosen section obtained by zero-field cooling to 30 K and then raising the field to 48 mT is shown in Fig. 3A, and Fig. 3B shows the corresponding contours of $H_z(x, y)$, plotted in increments of 4 mT. We applied our inversion of the Biot-Savart law to the data in Fig. 3B to calculate contours of the current stream function $F(x, y)$, which coincide with the current stream lines (Fig. 3C). Regions with a higher density of stream lines are those with higher local sheet currents $\mathbf{J}(x, y)$. The stream lines explicitly show how the high-angle colony boundaries at b and c cause $\mathbf{J}(\mathbf{r})$ to deviate locally from the sample axis. The characteristic T-shaped channel at c in Figs. 1A and 3A corresponds to a high-angle colony boundary that is a strong but only partial barrier to current flow (*7*). Thus, large currents flow locally on either side of the boundary, but the current crossing c is greatly reduced, consistent with the lowered transport J_c between V2 and V3. A similar but lesser disturbance of $\mathbf{J}(\mathbf{r})$ occurs at b, where current bypasses a diagonal defect about half the width of the bridge. Notice that the current stream lines in Fig. 3C are quite different from the contours of $H_z(x, y)$ in Fig. 3B, which is a specific feature of the

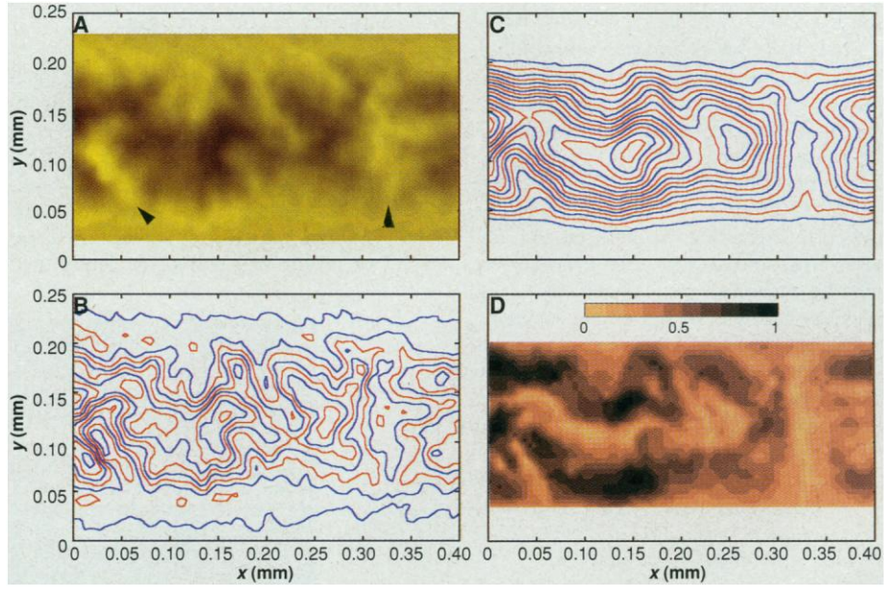

Fig. 3. (**A**) MO image of the region between the large blue arrows in Fig. 1 (defects b and c in Fig. 1A are marked by black arrows here) after cooling it to 30 K in zero field and then applying a perpendicular field of 48 mT. Dark areas correspond to regions of lower magnetic field and stronger shielding. (**B**) Contours of the normal field component $H_z(x, y)$ derived from (A), plotted in increments of 4 mT. (**C**) Contours of the calculated sheet current stream function $F(x, y)$ plotted in increments of 4.5 × 10^3 A/cm. The contours coincide with the current stream lines. The red and blue colors were used to distinguish between the neighboring contours of $H_z(x, y)$ and $F(x, y)$. (**D**) A 2D color map of the reconstructed local $J_c(\mathbf{r})$ in the strip, plotted in increments of 10^5 A/cm^2, according to the scale shown in inset, where the numbers correspond to J_c in units of 10^6 A/cm^2. The lightest color corresponds to $0 < J_c < 10^5$ A/cm^2, and the darkest color corresponds to $J_c > 9 \times 10^5$ A/cm^2.

2D sheet geometry.

From the calculated current stream function $F(x, y)$ in Fig. 3C, we can obtain the distribution of local sheet critical current densities $J_c(\mathbf{r}) = [(\partial F/\partial x)^2 + (\partial F/\partial y)^2]^{1/2}$ (Fig. 3D). The values are highly nonuniform, ranging from 10^5 to 10^6 A/cm^2 on a length scale at least 10 times as large as the average grain size. The percolative nature of the current is clear, as is the high suppression of J_c within the colony boundaries. These boundaries themselves are quite nonuniform and exhibit noticeable variations in J_c across the bridge on the scale of tens of micrometers. An extended low-J_c region meanders along the center of the bridge, where current loops on a scale of many grain sizes tend to form. The local $J_c(\mathbf{r})$ values in Fig. 3D correspond to intergranular, not intragranular, currents because the characteristic length scale of 50 to 100 μm over which J_c changes is much larger than the 5- to 10-μm Tl-1223 grain size. Analogous results were obtained from images taken for other temperatures between 9 and 77 K. For instance, the local $J_c(\mathbf{r})$ at 77 K and 24 mT could exceed 2×10^5 A/cm^2, although the transport J_c of the bridge at 77 K and 0 T was reduced to 1.9×10^4 A/cm^2 by three colony boundaries.

REFERENCES AND NOTES

1. D. H. Kim *et al.*, *Physica C* **177**, 431 (1991).
2. E. D. Specht *et al.*, *ibid.* **242**, 164 (1995).
3. Y. Iijima, N. Tanabe, O. Kohno, Y. Ikeno, *Appl. Phys. Lett.* **60**, 769 (1992); X. D. Wu *et al.*, *ibid.* **67**, 2397 (1995).
4. D. C. Larbalestier *et al.*, in *Applied Superconductivity 1995* (Institute of Physics Conference Series Number 148, Institute of Physics, Philadelphia, 1995), vol. 1, pp. 29–34.
5. G. Blatter, M. V. Feigel'man, V. B. Geshkenbein, A. I. Larkin, V. M. Vinokur, *Rev. Mod. Phys.* **66**, 1125 (1994); E. H. Brandt, *Rep. Prog. Phys.* **58**, 1465 (1995); D. J. Bishop, P. L. Gammel, D. A. Huse, C. A. Murray, *Science* **255**, 165 (1992); H. Dai, S. Yoon, J. Liu, R. C. Budhani, C. M. Lieber, *ibid.* **265**, 1552 (1994).
6. D. Dimos, P. Chaudhari, J. Mannhart, *Phys. Rev. B* **41**, 4038 (1990); N. Heinig *et al.*, *Appl. Phys. Lett.* **69**, 577 (1996).
7. A. Polyanskii *et al.*, *Phys. Rev. B* **53**, 8687 (1996).
8. J. A. Parrell, A. A. Polyanskii, A. E. Pashitski, D. C. Larbalestier, *Supercond. Sci. Technol.* **9**, 393 (1996).
9. D. C. Larbalestier, *Proceedings of the 10th Anniversary HTS Workshop on Physics, Materials and Applications* (World Scientific, Rivers Edge, NJ, 1996), p. 41.
10. L. A. Dorosinskii *et al.*, *Physica C* **203**, 149 (1992); C. A. Duran *et al.*, *Nature* **357**, 474 (1992); Th. Schuster, M. R. Koblischka, B. Ludescher, H. Kronmuller, *J. Appl. Phys.* **72**, 1478 (1992); N. Nakamura, G. D. Gu, K. Takamuku, M. Murakami, N. Koshizuka, *Appl. Phys. Lett.* **61**, 3044 (1992).
11. A. E. Pashitski, A. Polyanskii, A. Gurevich, J. A. Parrell, D. C. Larbalestier, *Physica C* **246**, 133 (1995); *Appl. Phys. Lett.* **67**, 2720 (1995); U. Welp *et al.*, *Nature* **376**, 44 (1995); *Appl. Phys. Lett.* **66**, 1271 (1995).
12. M. Turchinskaya *et al.*, *Physica C* **216**, 205 (1993).
13. J. A. DeLuca *et al.*, *ibid.* **205**, 21 (1993).
14. E. D. Specht *et al.*, *ibid.* **226**, 76 (1994).
15. E. H. Brandt, *Phys. Rev. B* **46**, 8628 (1992).
16. B. J. Roth, N. G. Sepulveda, J. P. Wikswo Jr., *J. Appl. Phys.* **65**, 361 (1989).
17. P. D. Grant *et al.*, *Physica C* **229**, 289 (1994); W. Xing, B. Heinrich, H. Zhou, A. A. Fife, A. R. Cragg, *J. Appl. Phys.* **76**, 4244 (1994); H. Niculescu, A. Saenz, M. Khankhasayev, P. J. Gielisse, *Physica C* **261**, 12 (1996).
18. Reconstruction of 2D current flow patterns in thin films from MO images. The sheet current $\mathbf{J}(\mathbf{r})$ in thin films can be expressed by the stream function $F(x, y)$

$$J_x(x,y) = \frac{\partial F}{\partial y},\ J_y(x, y) = -\frac{\partial F}{\partial x} \quad (1)$$

The Fourier components $F(\mathbf{k})$ and $H_z(\mathbf{k})$ are related by the Biot-Savart law

$$H_z(k) = \frac{k}{2} e^{-k|z|} F(k) \quad (2)$$

where $k = |\mathbf{k}|$. For $z = 0$, the inverse Fourier transform of Eq. 2 yields

$$F(x, y) = \frac{1}{\pi} \int_{-\infty}^{\infty} \int_{-\infty}^{\infty} \frac{H_z(x',y')dx'dy'}{[(x - x')^2 + (y - y')^2]^{1/2}} \quad (3)$$

Equations 1 and 3 in principle enable the local current to be reconstructed from $H_z(x, y)$, obtained from the MO image. However, Eq. 3 requires integration of $H_z(x, y)$ over an infinitely large region, and $H_z(x, y)$ can only be measured in a finite domain, limited by the size of the MO film, the microscope field of view, and so forth. Moreover, the MO signal is measured at a nonzero distance $z_0 \sim 5$ μm above the surface, and $H_z(x, y)$ inevitably contains short-wavelength noise on a scale less than z_0 as a result of imperfections in the MO film. Because this noise produces fictitious "currents" in Eqs. 1 and 3, we used a noise reduction procedure (*15*), interpolating the digitized image signal by a spline and averaging it over a 6-μm by 6-μm grid. This suppresses irrelevant short-wave components of $H_z(x, y)$ by 7 to 10 times, without interfering with the larger scale variations of $H_z(x, y)$ caused by local inhomogeneities of $J_c(x, y)$. To avoid the restriction created by the finite area of $H_z(x, y)$ measurements, we rewrite Eq. 3 in the form

$$F(x, y) = \frac{1}{\pi} \int_{-b}^{b} dx' \int_{-a}^{a} \times \frac{[H_z(x',y') - H_0(y')]dy'}{[(x - x')^2 + (y - y')^2 + \aleph^2]^{1/2}} + F_0(y) \quad (4)$$

where $H_0(y)$ is the magnetic field that corresponds to the stream function $F_0(y)$, and the x axis is directed along the bridge. For infinite integration limits, Eq. 4 reduces to Eq. 3 for any $F_0(y)$. Now we choose $H_0(y)$ such that the main contribution to the integral in Eq. 4 comes from a $2b$ by $2a$ rectangle that includes the region of the bridge $|x| < 2w$, $|y| < w$, where $\mathbf{J}(\mathbf{r})$ was reconstructed ($2w$ is the bridge width). This can be done by taking $H_0(y)$, which gives the best fit to the measured $H_z(x, y)$ outside the sample ($|y| > w$), thus greatly improving the convergence of the integral in Eq. 4 and making it practically independent of a for $a > 2w$. We set $a = b = 4w$ and took $F_0(y)$ of the critical state model for a strip, for which $F_0(y) = J_{c0}(|y| - w)$ at $|y| \le w$, $F_0(y) = 0$ at $|y| > w$, and (*7*)

$$H_0 = \frac{J_{c0}}{\pi} \ln\left[\frac{(y^2 + z_0^2)^2}{(w^2 + y^2 + z_0^2)^2 - 4w^2y^2}\right] + H_a \quad (5)$$

Here H_a is the applied field, and the averaged critical current density J_{c0} was determined by fitting the measured $H_z(x, y)$ with Eq. 5 beyond the bridge, $w < |y| < 4w$, where the influence of local inhomogeneities in the films is weak. For instance, a current loop of size L produces a field $H(r) \propto L/r^2$ at distance $r \gg L$, so the contribution to $H_z(r)$ from typical inhomogeneities with $L \approx 0.1w$ to $0.3w$ at $r = 2w$ to $3w$ is only a few percent of $H_z(r)$ at $r = L$. Notice that a, b, and $F_0(y)$ in Eq. 4 are only auxiliary quantities to account for the long-range character of $H_z(x, y)$ for the sheet geometry (*19*). We made sure that $\mathbf{J}(\mathbf{r})$ calculated from Eqs. 1 and 4 is indeed insensitive to the specific choice of $F_0(y)$. The value $\aleph \sim z_0/2\pi$ in Eq. 4 accounts for $H_z(x, y)$ being measured at finite height z_0 and the fact that the Fourier components $F(k)$ with $k > 1/z_0$ should be excluded to avoid fictitious short-wavelength noise currents and thus to make the inversion scheme stable (*16*). We set $\aleph = 0.8$ μm, but because $\aleph$ is much smaller than the spatial resolution of our MO technique, the calculated $\mathbf{J}(\mathbf{r})$ only very weakly depends on $\aleph$.
19. E. H. Brandt and M. Indenbom, *Phys. Rev. B* **48**, 12893 (1993); E. Zeldov, J. R. Clem, M. McElfresh, M. Darwin, *ibid.* **49**, 9802 (1994).

20. The work at University of Wisconsin was supported by the NSF Materials Research Group Program (DMR 9214707) and the Electric Power Research Institute (RP 8009-5). The work at Oak Ridge National Laboratory is managed by Lockheed Martin Energy Research for the U.S. Department of Energy (DOE) under contract DE-AC05-96OR22464. The work was partly conducted at the National Synchrotron Light Source, which is supported by DOE under contract DE-AC02-76CH00016.

26 August 1996; accepted 27 November 1996

Hillslope Evolution by Bedrock Landslides

Alexander L. Densmore,* Robert S. Anderson, Brian G. McAdoo, Michael A. Ellis

Bedrock landsliding is a dominant geomorphic process in a number of high-relief landscapes, yet is neglected in landscape evolution models. A physical model of sliding in beans is presented, in which incremental lowering of one wall simulates baselevel fall and generates slides. Frequent small slides produce irregular hillslopes, on which steep toes and head scarps persist until being cleared by infrequent large slides. These steep segments are observed on hillslopes in high-relief landscapes and have been interpreted as evidence for increases in tectonic or climatic process rates. In certain cases, they may instead reflect normal hillslope evolution by landsliding.

Bedrock landsliding is an important process in the evolution of diverse landscapes (*1–5*). Most models of landscape evolution, however, assume that diffusive processes shape hillslopes (*4*, *6*) or that slopes are instantaneously lowered above some threshold (*7*). Likewise, models of bedrock landslides have ignored long-term hillslope evolution by discrete events (*8–11*).

Several factors argue for the inclusion of discrete landslides in landscape evolution models. First, rates of landscape evolution